THESIS

MODELING HYDROLOGIC PROCESSES ASSOCIATED WITH SOIL SATURATION AND DEBRIS FLOW INITIATION DURING THE SEPTEMBER 2013 STORM, COLORADO FRONT RANGE

Submitted by

Sujana Timilsina

Department of Civil and Environmental Engineering

In partial fulfillment of the requirements

For the Degree of Master of Science

Colorado State University

Fort Collins, Colorado

Summer 2019

Master's Committee:

Advisor: Jeffrey D. Niemann

Sara L. Rathburn
Peter A. Nelson

ABSTRACT

MODELING HYDROLOGIC PROCESSES ASSOCIATED WITH SOIL SATURATION AND DEBRIS FLOW INITIATION DURING THE SEPTEMBER 2013 STORM, COLORADO FRONT RANGE

Seven days of extreme rainfall during September 2013 produced more than 1,100 debris flows in the Colorado Front Range, about 78% of which occurred on south-facing slopes (SFS). A few previously-published soil moisture observations suggest that SFS were wetter than north-facing slopes (NFS) during the event, which would contrast with soil moisture patterns observed during dry conditions. Various causes have been hypothesized for the preferential saturation of SFS, but those hypotheses remain largely untested. The objectives of this study are to analyze the soil moisture patterns using additional soil moisture observations, determine the hydrologic processes behind the preferential saturation of SFS, and to evaluate the importance of soil moisture in determining the debris flow initiation sites. Soil moisture patterns are simulated using the Equilibrium Moisture from Topography, Vegetation, and Soil (EMT+VS) model for a study region that includes 63% of the observed debris flow locations. Five hypotheses are implemented in the model including: (1) higher rainfall rates, (2) lower interception rates, (3) lower porosity, (4) thinner soils, and (5) reduced deep drainage on SFS. The EMT+VS model is also coupled with an infinite slope stability model to produce factor of safety maps. The hypotheses are tested by comparing the modeled soil moisture patterns to soil moisture observations and the debris flow initiation sites. The results suggest that differences in interception and deep drainage between the slopes were primarily responsible for producing

wetter SFS, but the soil moisture pattern likely played a smaller role than vegetation and slope in determining the debris initiation sites.

ACKNOWLEDGMENTS

I would like to express my sincere gratitude to my advisor Dr. Jeffrey D. Niemann for his guidance and continuous support in this research. I would also like to thank Dr. Sara L. Rathburn and Dr. Francis K. Rengers for their helpful suggestions and feedback in this research. I would also like to thank Dr. Peter Nelson for his support and suggestions. I am also very thankful to the IIE's Fulbright Program for providing me financial support and a wonderful opportunity to be a part of Colorado State University. Finally, I am forever grateful for the support from my parents in my every step of life.

TABLE OF CONTENTS

1. INTRODUCTION

During 9-16 September 2013, heavy rainfall occurred in the Colorado Front Range with total rainfall exceeding 450 mm in some locations (Gochis et al., 2015). The extreme rainfall occurred from Boulder in the south to Estes Park in the north, and the most heavily affected watersheds were the Boulder, Saint Vrain, Little Thompson, and the southern part of the Big Thompson (Gochis et al., 2015). The resulting flooding and debris flows caused 8 fatalities and damage exceeding 2 billion U.S. dollars (Gochis et al., 2015).

This event produced at least 1138 debris flows and 212 rock, earth, and debris slides in the region (Coe et al., 2014). The debris flows started after the most intense rainfall period (12.5 hr during 11-12 September 2013) (Coe et al., 2014), and 78% of the debris flows were initiated on south-facing slopes (SFS) (Coe et al., 2014). Debris flows were more common on SFS in part because less vegetation cover exists on those hillslopes. Vegetation varies with aspect in the Front Range (Marr, 1961). Dense forest stands occur on north-facing slopes (NFS), while sparser trees, shrublands, and grasses occur on the SFS (Ebel, 2013). By comparing the density of the debris flow sites to an index that quantifies the vegetation greenness, Rengers et al. (2016) found that debris flows occurred more frequently at sites with lower vegetation density irrespective of hillslope orientation.

Soil moisture might have also contributed to the debris flow initiation pattern. Limited published data suggest that saturation was more frequent on SFS during the storm. Specifically, Ebel et al. (2015) considered the soil moisture at seven sites east of Sugarloaf Mountain including NFS and SFS as well as burned and unburned sites. Their observations show that the SFS saturated briefly at both the burned and unburned sites, while the NFS did not reach

saturation at any site. If that pattern was widespread throughout the Front Range, it would contrast with soil moisture patterns that have been observed during more typical dry conditions. Coleman and Niemann (2013) presented soil moisture observations from 350 locations on 9 dates in the 8 ha Cache la Poudre experimental catchment in the northern Front Range. They found that NFS were typically wetter than SFS. Similar results were observed by Traff et al. (2015) using a long-term dataset from fewer observation sites. If the soil moisture pattern reversed during the storm, it would suggest that the soil moisture patterns are temporarily unstable, a property that has been observed in other regions but not for the Front Range (Coleman and Niemann, 2013;Western et al., 1999).

Several studies have proposed potential reasons for the more frequent saturation of SFS during the storm. Coe et al. (2014) suggested that the northwestward moving storm might have produced more intense rainfall on the south- and east-facing slopes. This higher rainfall rate might have promoted saturation and helped trigger the debris flows. Lower interception rates on SFS due to the aspect-dependent vegetation has also been suggested (Rengers et al., 2016; Valante et al., 1997). Variations in soil depth have been suggested as another possible cause (Coe et al., 2014). Soils are usually thinner on SFS than NFS (McGuire et al., 2016; Smith et al., 2011), which could reduce the soil's capacity to accept throughfall without saturating. Porosity variations have also been proposed as a factor. Ebel et al. (2015) suggested that large stone fragments in the soil on SFS may reduce the effective porosity and water storage capacity on SFS. Finally, reduced deep drainage has also been suggested as a possible cause. Ebel et al. (2015) suggested that the sparser vegetation on SFS may result in less weathering of the underlying bedrock and thus less vertical drainage from the soil to the shallow groundwater in the saprolite layer.

McGuire et al. (2016) examined some of these hypotheses for an area adjacent to North Saint Vrain Creek. HYDRUS-1D was used to simulate soil moisture and an infinite slope stability model was used to estimate the factor of safety (FOS) for represenative NFS and SFS. The effects of variations in soil depth, interception, deep drainage, and root reinforcement were tested using different model scenarios. Their results indicate that root reinforcement was the primary reason for the stability of the NFS. However, the study was focused in an area of 0.25 km^2 within the Front Range and did not consider all the hypotheses. It also primarily focused on slope stability rather than the soil moisture pattern.

The main objectives of the present research are: (1) to determine if saturation was more common on SFS using additional soil moisture observations, (2) to assess the hydrologic mechanisms that produced preferential saturation on SFS, and (3) to evaluate the importance of the soil moisture pattern in determining the pattern of debris flow initiation throughout the Front Range. To accomplish these objectives, soil moisture observations are analyzed from two study regions: the Cache la Poudre catchment and the Boulder Creek Critical Zone Observatory (CZO). We then apply the Equilibrium Moisture from Topography, Vegetation, and Soil (EMT+VS) model to generate soil moisture patterns. Five hypotheses are implemented in the model in separate scenarios including: (1) higher rainfall rates, (2) lower interception rates, (3) lower porosity, (4) thinner soils, and (5) reduced deep drainage on SFS. The EMT+VS model output is also used in an infinite slope stability model to generate FOS maps. The results are then compared to the available soil moisture observations and mapped debris flow initiation sites.

The outline of this document is as follows. Section 2 describes all the study's materials and methods including the study region, the available observations, and the two models. Section 3 describes how the two models are applied including their inputs and parameter values. Section

4 summarizes both the soil moisture and FOS results, and Section 5 summarizes the main conclusions.

2. MATERIALS AND METHODS

2.1 Study Regions and Available Observations

Figure 1(a) shows the observed debris flow initiation sites along with our overall study region. The debris flows occurred in an area of 3430 km^2 in the Colorado Front Range (Gochis et al., 2015). Coe et al. (2014) identified these debris flow initiation sites by field inspections and using 0.5 m resolution orthorectified satellite imagery from the Digital Globe Inc. Patton et al. (2018) also identified 11 debris flows in Rocky Mountain National Park with field observations. Our overall study region was determined by the grid cell boundaries of the coarse-resolution soil moisture input to the EMT+VS model (see further discussion below). The study region includes the Little Thompson, Saint Vrain, Boulder, Lefthand, and Fourmile watersheds as well as the southern part of the Big Thompson watershed. The region includes approximately 63% of the mapped debris flows.

The meteorological properties of the study region were characterized using data from two sources. Daily precipitation and potential evapotranspiration (PET) data were obtained for a 10-year period (2003-2013) from 16 weather stations in the Global Historical Climatology Network (accessed through the Utah Climate Center website). These weather stations range from 1594 m to 3139 m in elevation (Figure 1a). The provided PET was calculated using the temperature-based Hargreaves equation. Daily average wind speed and direction data were obtained for the same 10-year period from 5 stations in the Western Regional Climate Center's Remote Automated Weather Station (RAWS) network. These stations span 1854 m to 2500 m in elevation (Figure 1a).

2.1.1 Cache la Poudre Catchment

Soil moisture observations are analyzed from the Cache la Poudre catchment (Traff et al., 2015). This catchment is located near Rustic, Colorado (Figure 1a). Although it is north of the main study region, the edge of the storm still reached this area. The catchment has an area of approximately 8 ha, an average elevation of 2193 m, and a total relief of 115 m. Its mean annual precipitation is about 400 mm. The vegetation is aspect-dependent with coniferous forest (ponderosa pine) dominating the NFS and shrublands (mountain mahogany and antelope bitterbrush) dominating the SFS. No recent fire has occurred in this catchment. Hourly soil moisture data in the top 5 cm of the soil are available for the storm from 22 time-domain reflectometry (TDR) probes. These probes were distributed between the SFS and NFS (Figure 1b). Most probes were positioned under representative ponderosa pine, mountain mahogany, and antelope bitterbrush plants, but two probes were positioned in inter-canopy locations. Rainfall was also measured at an inter-canopy location on each hillslope. From 9 September 2013 to 13 September 2013, 137 mm and 149 mm of rainfall were measured on the NFS and SFS, respectively. Throughfall measurements are also available from under a representative antelope bitterbrush shrub and ponderosa pine tree.

2.1.2 Boulder Creek Critical Zone Observatory (CZO)

The Boulder Creek CZO lies in the Boulder Creek watershed. Soil moisture data from the Betasso and Gordon Gulch areas are used in this study. Gordon Gulch includes Lower and Upper Gordon Gulch (Figure 1c), and the elevation ranges from 2440 m to 2740 m with a mean annual precipitation of approximately 500 mm. The NFS are densely forested, while the SFS have fewer trees and more shrubs. Betasso lies in lower Boulder Canyon. Its elevation ranges from 1810 m

to 2024 m, and its mean annual precipitation is approximately 400 mm. The NFS has a ponderosa pine and Douglas fir mix, while the SFS has ponderosa pine trees (White et al., 2015). Soil moisture measurements are available from 10 sites in the Boulder Creek CZO including 8 sites in Lower Gordon Gulch, 1 site in Upper Gordon Gulch, and 1 site in Betasso (Figure 1c). The 8 sites in the Lower Gordon Gulch include 3 sites on NFS, 4 sites on SFS, and 1 flat site. The Upper Gordon Gulch site is on a NFS (northeast facing), whereas the Betasso site is on a SFS. Most observations were collected with Campbell Scientific CS616 soil moisture sensors, and the observation depths vary between sites but range from 5 cm to 138 cm (Anderson et al., 2018).

2.2 Modeling Methods

2.2.1 Soil Moisture

The EMT+VS model is a soil moisture downscaling method. It accepts coarse-resolution soil moisture as input and infers fine-scale soil moisture patterns based on fine-scale topographic and vegetation data (fine-scale soil data can be accepted if available). The EMT+VS method is used because it has been previously calibrated and tested for the Cache la Poudre catchment (Ranney et al., 2015) as well as several other catchments, watersheds, and regions (Cowley et al., 2017; Grieco et al. 2018; Ranney et al., 2015). It also explicitly considers soil moisture's dependence on topography, vegetation, and soil and is able to reproduce temporally unstable soil moisture patterns (Coleman and Niemann, 2013). Detailed derivations and descriptions of the model are provided by Cowley et al. (2017) and Ranney et al. (2015), so only a brief summary is provided here.

The EMT+VS model is based on the water balance of the soil layer. It assumes equilibrium, so it cannot capture hysteresis in the soil moisture patterns. It also neglects temporal variations in most regional characteristics, such as the vegetation cover. The soil moisture is assumed to be uniform with depth in the soil layer, and the following processes are included in the water balance: infiltration, deep drainage, lateral flow, and evapotranspiration (ET). The infiltration is determined by considering orographic precipitation variations as well as interception by the vegetation (Cowley et al., 2017). The resulting equation is:

$$F = \overline{P}\frac{\left[1+\tau(Z_{\#}-\overline{Z}_{\#})\right]\left\{1+\xi\left[S_{\#}\cos(R_{\#}-\upsilon)-\overline{S_{\#}\cos(R_{\#}-\upsilon)}\right]\right\}}{1+\tau\xi\left[\overline{Z_{\#}S_{\#}\cos(R_{\#}-\upsilon)}-\overline{Z}_{\#}\,\overline{S_{\#}\cos(R_{\#}-\upsilon)}\right]}\left(1-\lambda V\right) \quad (1)$$

where F is the infiltration rate, $\overline{P}$ is the spatial-average precipitation (which eventually cancels out of the model solution), τ controls the elevation dependence of precipitation, ξ controls the orientation dependence of precipitation, υ is the direction from which all topographic orientations are calculated. The variables $Z_{\#}$, $S_{\#}$, and $R_{\#}$ are the elevation, slope, and aspect which are all calculated from a digital elevation model (DEM) at the spatial scale of the orographic effect. λ describes the vegetation's interception efficiency, and V is the fractional vegetation cover, which is determined from Landsat data (see later discussion). Overbars in all equations indicate averages over the spatial extent of the coarse-resolution soil moisture grid cells.

The deep drainage is calculated from Darcy's Law by assuming that gravity dominates the hydraulic gradient and that the Campbell (1974) equation defines the unsaturated hydraulic conductivity. The resulting equation is:

$$G = K_{s,v}\left(\frac{\theta}{\theta_s}\right)^{\gamma_v} \tag{2}$$

where G is the deep drainage, $K_{s,v}$ is the vertical saturated hydraulic conductivity, θ is the soil moisture (volumetric water content), θ_s is the soil porosity, and γ_v is the vertical pore disconnectedness index.

The lateral flow is calculated from Darcy's Law using the Campbell (1974) equation, a soil thickness that can depend on topographic curvature, and the assumption that the lateral hydraulic gradient is a function of the topographic slope. The resulting equation is:

$$L = \delta_0\left(\frac{\kappa_{\min} - \kappa}{\kappa_{\min}}\right) c\iota K_{s,v}\left(\frac{\theta}{\theta_s}\right)^{\gamma_h} S^{\varepsilon} \tag{3}$$

where L is the lateral flow, δ_0 is the soil depth where the topographic curvature is zero, $\kappa_{\min}$ is the minimum topographic curvature for which the soil layer is present, and κ is the topographic curvature, c is the linear dimension of the fine-resolution soil moisture, which matches the resolution of the DEM. ι is the anisotropy of the soil, γ_h is the horizontal pore disconnectedness, S is the topographic slope, and ε relates the lateral hydraulic gradient to the topographic slope.

The ET expression is determined by accounting for any elevation dependence of and partitioning the potential ET into potential evaporation and potential transpiration based on the fractional vegetation cover V. It uses the Priestley-Taylor (1972) assumption and power functions to describe the effects of limited soil moisture on the ET rate. Shading effects are also incorporated for the soil evaporation, and root-water uptake can occur from non-modeled layers. The resulting expression is:

$$E = \bar{E}_p \left[1 + \omega\left(\bar{Z} - Z\right)\right]\left[\eta V + \left(1 - V\right)^{\mu}\right]\left[\frac{I_p}{1+\alpha}\left(\frac{\theta}{\theta_s}\right)^{\beta_r} + \frac{\alpha}{1+\alpha}\left(\frac{\theta}{\theta_s}\right)^{\beta_a}\right] \quad (4)$$

where E is the ET, $\bar{E}_p$ is the spatial-average PET, ω controls the elevation dependence of PET, η is the portion of the transpiration that occurs from the modeled soil layer, μ describes the shading effect, α is the Priestly-Taylor coefficient minus one, I_p is the potential solar radiation index (determined from the DEM), and β_r and β_a control the moisture limitation effects on the radiative and aerodynamic terms of ET, respectively.

The solution of the water balance equation was developed and tested by Coleman and Niemann (2013) and Ranney et al. (2015). The fine-resolution soil moisture θ is calculated as:

$$\theta = \frac{w_G\theta_G + w_L\theta_L + w_R\theta_R + w_A\theta_A}{w_G + w_L + w_R + w_A} \quad (5)$$

where θ_G, θ_L, θ_R, and θ_A are analytical estimates of the soil moisture if deep drainage, lateral flow, radiative ET, and aerodynamic ET dominate the water balance, respectively. The variables w_G, w_L, w_R, and w_A are weights that control the importance of θ_G, θ_L, θ_R, and θ_A to the final estimate of θ. The weights depend on the model parameters and the coarse-resolution soil moisture input.

2.2.2 Slope Stability

From an analysis of more than 500 articles related to landslide susceptibility modeling, Reichenbach et al. (2018) found that physically- and statistically-based methods are preferred for quantitatively determining the landslide occurrence. Physically-based infinite slope stability models have been widely used with hydrological models to determine landslide susceptibility

(e.g., Carrara et al., 2008; Montgomery & Dietrich, 1994; Reichenbach et al., 2018). Due to its simplicity and previous application in this region by McGuire et al. (2016), Lu and Godt's (2008) infinite slope stability model is used for this study.

Lu and Godt (2008) provide a detailed discussion of the slope stability model, so only a brief summary is provided here. The slope stability FOS is calculated as the ratio of net forces driving downslope movement to net forces holding the soil in place. The FOS F_s is given as:

$$F_s = \frac{\tan\phi}{\tan T} + \frac{2C}{\gamma_s \delta \sin 2T} - \frac{\sigma_s}{\gamma_s \delta}\left(\tan T + \cot T\right)\tan\phi \tag{6}$$

where ϕ is the friction angle, T is the topographic slope angle ($\tan T$ is equivalent to S in the EMT+VS model), C is the bulk cohesion, γ_s is the unit weight of the soil, δ is the soil thickness, σ_s is the suction stress. The first term of the equation incorporates the stability due to the internal frictional resistance of the soil. The second term includes the bulk cohesion which can be further expressed as:

$$C = C_s + C_v \tag{7}$$

where C_s is the cohesion of the soil itself and C_v is the cohesion due to vegetation. The third term includes the suction stress which is given by:

$$\sigma_s = \frac{\theta - \theta_r}{\theta_s - \theta_r}\psi\gamma_w \tag{8}$$

where θ_r is the residual soil moisture, ψ is the suction head at soil moisture θ, and γ_w is the unit weight of water. In the present study, the suction is determined using the Campbell (1974) equation:

$$\psi = \psi_s\left(\frac{\theta_s}{\theta}\right)^b \tag{9}$$

where ψ_s is the matric potential at saturation and b is the pore size distribution index.

3. MODEL APPLICATION

3.1 EMT+VS Inputs

The required topographic attributes were derived from a 1/3 arc second DEM from the U.S. Geological Survey's National Map. The DEM was resampled to 10 m using the nearest neighbor method in ArcGIS. The nearest neighbor approach is used instead of an interpolation method because it retains the steep slopes that can be important for debris flow initiation. The flow directions were calculated using the D-infinity method, and other topographic attributes such as slope, aspect, and contributing area, were calculated using TauDEM (Tarboton, 2003) and the spatial analyst tools in ArcGIS.

Fractional vegetation cover was derived from Normalized Difference Vegetation Index (NDVI) data from Landsat 5. NDVI from 28 September 2011 was used because that date is cloud-free and occurs at about the same time of year as the storm. The fractional vegetation cover was determined from the NDVI as (Montandon and Small, 2008):

$$V = \frac{NDVI - NDVI_0}{NDVI_\infty - NDVI_0} \tag{10}$$

where $NDVI$ is the NDVI value for the cell, $NDVI_0$ is the bare soil NDVI, and $NDVI_\infty$ is the NDVI for a cell that is fully covered with live vegetation. For the study region, $NDVI_0 = 0.04$ was found for cells that are bare in satellite photos, and $NDVI_\infty = 0.70$ was found for densely-vegetated cells in the satellite photos. Matsui et al. (2005) previously used $NDVI_\infty = 0.67$ for the evergreen forests in North America, and Zeng et al. (2000) used $NDVI_\infty = 0.68$ for mixed forests in the Conterminous United States (Montandon and Small, 2008).

Coarse-resolution soil moisture data were obtained from the North American Land Data Assimilation System (NLDAS) (NCEP/EMC 2009; Xia et al., 2012) because the storm pre-dates Soil Moisture Active Passive satellite data. Within NLDAS, soil moisture is generated by four land-surface models: Noah, Mosaic, Sacramento Soil Moisture Accounting, and Variable Infiltration Capacity. Xia et al. (2015) compared the soil moisture from these models to observations in the North American Soil Moisture Database for several U.S. states. Among the available models, Mosaic showed the best performance for Colorado (Xia et al., 2015), so its soil moisture is used as the coarse-resolution input to the EMT+VS model. The Mosiac model provides hourly soil moisture at a 0.125 degree resolution for 0-10 cm and 0-40 cm depths. The 0-40 cm depth was used to better match the observed soil depths in the Front Range (see later discussion). Xia et al. (2015) estimated the root-mean squared error (RMSE) of Mosaic's soil moisture as 0.03 m^3m^{-3} for the 0-40 cm depth. However, when the coarse resolution soil moisture was compared to all the available soil moisture observations from the storm period, the NLDAS soil moisture had bias of 0.08 m^3m^{-3}, which was removed before its use in the EMT+VS model.

3.2 EMT+VS Scenarios

3.2.1 Base Scenario

Before implementing any of the mechanisms that might cause the reversal in the soil moisture pattern, a base scenario is implemented with the EMT+VS model. For this scenario, nearly all EMT+VS parameter values were obtained from a previous study at the Cache la Poudre catchment (Hoehn, 2016). Those parameter values were calibrated within physically realistic ranges using a collection of soil moisture patterns from 2008 (Coleman and Niemann, 2013). However, because lateral flow is unimportant for that dataset, some parameters are not

well constrained by that calibration. Thus, the lateral flow parameters ε, ι, and $\kappa_{\min}$ were all set to values that have been recommended for uncalibrated EMT+VS model application by Grieco et al. (2018). $\overline{E}_p$ was set to the average PET from the 16 weather stations in the Front Range so it is more representative of the whole region. The orographic PET parameter ω was also determined using the PET data. For each weather station, the average PET during the entire 10-year observation period and the main storm period (9-13 September 2013) were plotted against elevation (Figure 2. (a) Annual average PET and (b) storm-period average PET vs. elevation for the weather stations in the Front Range.). The slopes of these plots provide estimates of ω. The two periods give similar ω values, but ω value for the storm period is used in the model. The soil depth δ_0 was also set to the average soil depth for NFS and SFS reported by McGuire et al. (2016) to be more representative of the larger region. Similarly, the vertical saturated hydraulic conductivity $K_{s,v}$ was set as the average hydraulic conductivity for NFS and SFS in Lower Gordon Gulch from Hinckley et al. (2014). For the base scenario, the orographic precipitation parameters (τ, υ, and ξ) and the interception efficiency parameter λ were set to 0 to initially neglect these phenomena. The complete set of parameter values for the base scenario is shown in Table 1. EMT+VS model inputs and parameters for different scenarios

3.2.2 Precipitation

To test the hypothesis that SFS received more rainfall than NFS, the orographic precipitation parameters (τ, υ, and ζ) were determined from the rain gauge data. To determine υ, the wind direction data were analyzed for the 10-year observation period and the storm period. For each case, a histogram was developed to determine the wind direction with highest

frequency of occurrence. The most common wind direction for the 10-year period was 274°, while the prevailing wind direction during the storm was 145°. The wind direction for the storm period was used for υ. This direction could support the notion that SFS received more rainfall than NFS if the orientation dependence was significant.

The parameters τ and ξ characterize the elevation and orientation dependence of the rainfall, respectively. The average precipitation rates during the 10-year observation period and the storm period were calculated from the weather stations. Those rates were then plotted against the orographic elevation $Z_{\#}$ and orientation $S_{\#}\cos\left(R_{\#}-\nu\right)$. Those topographic attributes were calculated using a 7-km spatial scale as suggested by several studies in other regions (Daly et al., 1994; Sharples et al., 2005; Thornton et al., 1997). For example, Cowley et al. (2017) showed that the strongest relationship between precipitation and elevation or orientation occurs at the 7-km scale for Reynold Creek in Idaho. For both periods of analysis, the average precipitation exhibits clear dependences on elevation. For the 10-year period (Figure 3a), it increases with elevation. During the storm period (Figure 3b), the average rainfall rate decreases with elevation, which is consistent with the relative abundance of debris flows at low elevations in the Front Range (Figure 1a). It is also consistent with Jarrett (1990), who found that major rainfall-induced flooding is rare at elevations above 2,300 m. No clear relationship is observed between the precipitation and orientation either for the 10-year period or the storm period. The values of τ, ξ, and υ for the storm period were used for the orographic precipitation scenario (Table 1).

3.2.3 Interception

To test the interception hypothesis, the base scenario was modified to include a non-zero interception efficiency λ, which was estimated from the rainfall and throughfall data in the

Cache la Poudre catchment during the storm. In the EMT+VS model, the fraction of rainfall that is intercepted I is:

$$I = \lambda V \tag{11}$$

The interception fraction was calculated from the rainfall and throughfall data as 9.7% for the SFS and 42% for the NFS. These values are surprisingly large and might have occurred due the low intensity and long duration of the 2013 storm. Lower interception fractions may have occurred where the storm was more intense, but no other throughfall observations are available. When accounting for the fractional vegetation cover in the grid cells where the throughfall data were collected, λ was found to be 0.75.

3.2.4 Soil Depth

Soils are known to be thicker on NFS where the vegetation density is higher (Geroy et al., 2011; Smith et al., 2011). McGuire et al. (2016) reported 0.64 m soil depth on NFS and 0.56 m on SFS for the area near North Saint Vrain Creek. For the soil depth hypothesis, the soil depth δ_0 throughout the region is estimated as a linear function of the fractional vegetation cover V. The linear function is set so that $\delta_0 = 0.56$ m for bare locations ($V = 0$) and $\delta_0 = 0.64$ m for fully-vegetated locations ($V = 1$). This approach assumes that vegetation is the underlying cause for the soil depth variation. Weathering rates and thus soil production depend strongly on the vegetation cover (Egli et al., 2008; Nikiforoff, 1949; Wilson, 2004).

3.2.5 Porosity

Porosity can be higher on NFS than SFS due to fewer coarse fragments on NFS compared to SFS. Geroy et al. (2011) reported higher porosity values for NFS ($\theta_s = 0.51$) than

SFS (θ_s = 0.41) in the Dry Creek watershed, north of Boise, Idaho. However, McGuire et al. (2016) used the same porosity value (θ_s = 0.41) for both NFS and SFS in their study in the Front Range. To test the porosity hypothesis, a spatially varying ϕ is added to the base scenario. Similar to the soil depth hypothesis, θ_s is estimated as a linear function of V (again assuming that vegetation is a key reason for the soil differences). The linear function is specified so that θ_s = 0.41 when $V = 0$ and θ_s = 0.51 when $V = 1$.

3.2.6 Deep Drainage

Thickly-vegetated NFS are expected to have greater deep drainage due to greater bedrock weathering (Anderson et al., 2011; Rempe & Dietrich, 2014). In addition, the saturated hydraulic conductivity is known to be influenced directly by vegetation (Berglund et al., 1980; McCulloch and Robinson, 1993) and the root mass for well-developed root systems (Archer et al., 2002; Petersson et al., 1987; Rasse et al., 2000). Hinckley et al. (2014) found saturated hydraulic conductivity to be greater on SFS than NFS near the surface (0-10 cm depth) at Lower Gordon Gulch. However, deeper in the soil (10-25 cm depth) the conductivity was larger for NFS than SFS. We calculated effective saturated hydraulic conductivities for the entire 0-25 cm depth using the values from Hinckley et al. (2014). The effective values are 556 mm/day for SFS and 4501 mm/day for NFS. For the deep drainage hypothesis, the vertical saturated hydraulic conductivity $K_{s,v}$ is estimated as a linear function of V so that $K_{s,v}$ = 556 mm/day when $V = 0$ and $K_{s,v}$ = 4501 mm/day when $V = 1$.

3.3 Slope Stability Model Inputs

For the slope stability model, the friction angle ϕ was determined from McGuire et al. (2016). They reported ϕ to be 29° for SFS and 31° for NFS. Given that this difference is small, ϕ was set to 30° throughout the region. The cohesion from vegetation C_v was estimated as a linear function of V because the vegetation cover has been shown to affect slope stability through root strength (Ziemer, 1981; Wu et al., 1979; Coppin, 1990). The selected linear function implies C_v = 0 kPa when $V = 0$ and C_v = 6.2 kPa when $V = 1$ based on Gray and Megahan (1981). The resulting C_v values for areas with shrubs and grasses were found to be similar to the range 1.6 – 2.1 kPa, which was suggested by Schmidt et al. (2001). The soil cohesion C_s was determined using a back-calculation method. In particular, the FOS was first calculated assuming C_s = 0 and using a soil moisture of 0.25 m^3m^{-3} at all locations. This soil moisture value was the highest observed soil moisture that occurred during the storm before the period when debris flows began initiating. For any location where the FOS was less than one, C_s was calculated to make the FOS = 1. Similar back-calculation methods are widely used to determine the soil strength parameters (Tang et al., 1999; Tiwari et al., 2005; Zhang et al., 2009). Ebel et al. (2015) assumed the residual water content θ_r to be zero for a study area at the 2010 Fourmile Canyon fire based on the previous study at the same site where the residual water content for unburned NFS and SFS was very low (0.01 and 0.03, respectively) (Ebel, 2012). θ_r is neglected in the EMT+VS model formulation, so θ_r set to 0 in this study as well. The spatially variable matric potential at saturation ψ_s is determined from the Cosby et al. (1984) pedotransfer functions using the soil texture properties from the Gridded Soil Survey Geographic Database (gSSURGO).

4. RESULTS

4.1 Soil Moisture at Observation Locations

Figure 4 shows measured soil moisture for sites on NFS and SFS for the Cache la Poudre catchment and the Boulder Creek CZO. For the Cache la Poudre catchment, the measurements are from the inter-canopy locations. For the Boulder Creek CZO, representative sites from Lower Gordon Gulch are shown. The dry period (left side of figure) is 6-9 September 2013 for the Boulder Creek CZO and 6-9 August 2013 for the Cache la Poudre catchment (soil moisture data are unavailable immediately before the storm at this site). During the dry period before the storm, the NFS is wetter in both regions, although the soil moisture is similar between NFS and SFS for the Cache la Poudre catchment. This behavior is consistent with soil moisture observations from other dry periods (Ranney et al., 2015; Traff et al., 2015). During the wet period during the storm (11-14 September 2013; right side of figure), the pattern reverses. In both regions, the NFS was substantially wetter than the SFS. This behavior is consistent with the observations during the storm from the area east of Sugarloaf Mountain (Ebel et al., 2015), and the changing structure indicates that the soil moisture patterns are temporally unstable.

We further evaluated whether the observation locations on NFS were more likely to reach saturation than locations on the SFS during the storm. Saturation was inferred if a site's soil moisture remained at a high constant value for a prolonged period. For the Cache la Poudre dataset, about 45% of the SFS locations saturated, but only about 9% of the NFS locations saturated during the storm. Similarly, for the Boulder Creek CZO dataset, approximately 40% of SFS sites and no NFS saturated during the storm. These results also confirm the observation from Ebel et al. (2015) that SFS were more likely to saturate during the storm.

The observed soil moisture values were also used to evaluate the soil moisture patterns from the EMT+VS model. For the Cache la Poudre catchment, multiple soil moisture observations were often collected within a single grid cell of the EMT+VS model. Also, the soil moisture data were collected for pre-selected conditions (e.g., under a particular species of shrub or tree) and thus are not necessarily representative of the average soil moisture for that grid cell. Similarly, at the Boulder Creek CZO, observations are available at multiple but varying depths at each location. Thus, it is difficult to make a quantitative evaluation of the EMT+VS model based on these observations.

Figure 5 graphically compares the EMT+VS model results for all scenarios to the range of soil moisture values observed within the given grid cell. The top part of the figure shows the results from the only grid cells with observations in the Cache la Poudre catchment, while the bottom shows the results for the representative locations in Lower Gordon Gulch that were previously shown in Figure 4. The left side shows the results for the NFS, while the right side shows the results for the SFS. In most cases, the range of observed values within each grid cell is wide due to the diversity of conditions that were observed. In contrast, the difference between the EMT+VS model scenarios is small at these particular locations. Other locations in the Front Range change more between the scenarios (see later results). At the Cache la Poudre catchment, the EMT+VS model results consistently fall within the range of the observations. At the Boulder Creek CZO, the EMT+VS model results fall within the observed range for the NFS, but they are lower than the observed range for the SFS. Among the 8 sites in the Boulder Creek CZO that are not shown, the model was within the observed range of moisture values for 6 sites and overestimated the soil moisture at 2 sites. It should be noted that the model was not calibrated to any of these observations, and the model is being applied over a very large region.

4.2 Soil Moisture Across Study Regions

The EMT+VS model was used to examine how the soil moisture patterns change between the dry and wet states when the five hypotheses are implemented. The dry state is represented by the soil moisture pattern at 23:00 on 8 September 2013, which is immediately before the storm began. The average coarse-resolution soil moisture at this time was 0.07 m^3m^{-3}. The wet state is represented by the soil moisture at 00:00 on 12 September 2013. At this time, the average coarse-resolution soil moisture over the study area was 0.27 m^3m^{-3}, which is among the wettest values during the storm. This time also roughly aligns with the occurrence of many of the debris flows.

Figure 6 shows the EMT+VS soil moisture maps for an example sub-region in the Saint Vrain watershed (the location and size of this region is shown in Figure 1 (a). It is adjacent to North Saint Vrain Creek and few kilometers west of the McGuire et al. (2016) study area. This region was selected because it has large NFS and SFS and a relatively high concentration of debris flows. For the dry state, the NFS are wetter than the SFS for all scenarios. This pattern is consistent with the soil moisture observations discussed earlier. For the wet state, the soil moisture patterns exhibit a very different structure. In particular, the wetter locations now occur in valley bottoms instead of on NFS. The reason for this change can be seen in Figure 7. This figure shows the relative weights that are used in the EMT+VS model (Equation 5) to calculate the final soil moisture. These weights were obtained for the representative NFS location in Lower Gordon Gulch, but similar weights occur throughout the study region. For dry conditions, the aerodynamic and radiative ET solutions have the largest weights because those fluxes are the greatest in the water balance. Thus, the soil moisture pattern depends strongly on the pattern of ET. Because NFS are oriented away from the sun and have greater shading by vegetation, they

have less ET and are wetter. During wet conditions, deep drainage and lateral flow have the largest weights. Lateral flow moves water from hilltops to valley bottoms, so the valleys tend to be the wettest locations.

Figure 6 also allows a comparison of the wet-state soil moisture patterns for the different hypotheses to see what processes might promote saturation on SFS. For the base scenario (Figure 6a), the NFS and SFS are about equally wet. When orographic precipitation is introduced (Figure 6b), the soil moisture pattern in this sub-region remains almost unchanged. As discussed earlier, the orographic precipitation pattern depends primarily on elevation rather than orientation. Even though the dominant wind direction was from the southeast during the storm, the spatial scale at which the orientation matters (7 km) is too large for individual SFS to be wetter than individual NFS in the model. Hence, the soil moisture remains similar for NFS and SFS.

When interception is added to the base case (Figure 6c), the SFS becomes wetter on average than the NFS for the wet state. Interception produces a greater reduction in throughfall where the vegetation is thicker. Because the NFS have denser forests than the SFS, the NFS are drier. It is worth noting that interception also promotes dryness on the NFS for the dry state (comparing Figure 6a and 6c), but its impact is insufficient to overcome the opposing pattern produced by the ET. Thus, interception contributes to the reversal of the soil moisture pattern between dry and wet states.

Introducing spatial variability in the soil depth (Figure 6d) produces similar soil moisture patterns as in the base scenario. For the wet state, lateral flow is important and shallower soils on SFS exhibit greater soil moisture because the water is distributed over a smaller depth. However, the variation in depth is not sufficient to produce a visible difference in the soil moisture pattern between NFS and SFS.

When spatially variable porosity is added to the base case (Figure 6e), the wet-state results exhibit drier SFS and wetter NFS than the base scenario. Hence, the porosity variation reinforces the wetter conditions on the SFS that occur in the dry state. Both deep drainage and lateral flow are calculated using Darcy's Law and thus depend on the hydraulic conductivity. The unsaturated hydraulic conductivity depends on the ratio of the soil moisture to the porosity in the Campbell equation. When porosity is larger, the soil moisture must be larger for the outflows to balance the inflows in the water balance. This effect leads to wetter conditions where the porosity is higher (NFS).

When spatial variations in deep drainage are added to the base case (Figure 6f), the wet-state soil moisture is greater on the SFS than the NFS. In this scenario, the vertical saturated hydraulic conductivity is higher on the NFS than the SFS. Thus, drainage out of the soil layer is greater on the NFS than the SFS, which promotes drier conditions on the NFS. The spatial variation in saturated hydraulic conductivity does not impact the dry state pattern because deep drainage is not important for dry conditions. Thus, the spatial variation in deep drainage also contributes to the reversal of the soil moisture pattern between the dry and wet states.

The final scenario combines all the hypotheses together except for the porosity hypothesis (Figure 6g). The porosity variation was excluded because it reinforces the dry state pattern (contradicting the available soil moisture observations), and the porosity values that were used were reported by Geroy et al. (2011) for the Dry Creek watershed in Idaho (due to unavailability of porosity data in the Front Range). McGuire et al. (2016) also used a spatially constant porosity of 0.41 for both NFS and SFS in the Front Range. For the combined scenario, the dry-state pattern shows wetter NFS and drier SFS, while the wet-state pattern has wetter SFS than NFS. Hence, the combined scenario also reproduces the observed reversal of the soil

moisture structure. The reversal of the pattern occurs for an average soil moisture of approximately 0.2, which roughly coincides with the transition in weights that was shown in Figure 7.

4.3 Debris Flow Initiation

The soil moisture patterns from the different hypotheses were used to calculate FOS maps using the slope stability model. Because most of the debris flows occurred on 12 September 2013, the FOS maps were generated at 00:00 on 12 September 2013 (i.e. the wet state shown in Figure 6). Figure 8 shows the FOS maps for the Saint Vrain sub-region. The model suggests that the NFS was almost entirely stable, while many locations on the SFS exhibited instability. Thus, the model results are qualitatively consistent with the abundance of debris flows on SFS. All scenarios show less stability on the SFS because the vegetation is sparse on that slope, which reduces the cohesion. However, the scenarios that produced the soil moisture reversal show increased instability on the SFS compared to the other scenarios. The FOS maps have vertical stripes in them due to the use of the nearest neighbor resampling method used to project the DEM. These stripes disappear if a bilinear or cubic interpolation method is used, but those methods smooth the topography and lose the more extreme slopes.

Figure 9 shows the FOS map for the entire study region for the combined scenario. Overall, the model tends to identify instabilities on SFS at lower elevations in the Front Range (see Figure 1 for satellite image of the region). This structure qualitatively agrees with pattern of observed debris flow initiation sites in the region.

The performance of the model for the different scenarios was quantified by determining the percentage of the observed unstable areas that were predicted unstable by the model (true

positives) and the percentage of observed stable areas that were predicted stable by the model (true negatives). Reichenbach et al. (2018) states that using the grid cell resolution for the analysis of the landslides gives misleading results and suggests using a coarser resolution to capture the morphologic dependencies of landslides. As the Landsat data used in this study has a 30 m resolution, a buffer value of 30 m was selected. To determine the performance of the model, any point within the buffer distance from an unstable point is also considered unstable.

The model's performance over the entire study region is shown in Table 2. For the base scenario, the model predicts 69.6% of the observed unstable areas to be unstable. For the same scenario, the model predicts 91.1% of the observed stable areas as stable. The orographic precipitation and soil depth hypotheses produce similar results to the base scenario. Although orographic precipitation promotes wetter conditions at low elevations, the change in soil moisture is small and does not improve the model performance. The interception and deep drainage hypotheses predict instability at higher percentages of the observed debris flow locations because they reverse the soil moisture pattern. The combined case successfully predicts instability at the most observed debris flow locations, but it also predicts the lowest percentage of observed stable locations as stable. Its overall performance is still the best among the scenarios, but the improvement over the base scenario is small. This small improvement likely arises from two causes. First, it is likely that the modeled soil moisture patterns are not accurate throughout this large region. Most spatial variations in lithology were neglected due to data limitations, and the model was not calibrated to either the soil moisture observations during the storm or the debris flow locations. Second, because all scenarios explain a significant portion of the stable and unstable locations, modeled factors other than the soil moisture reversal play a significant role in explaining the debris flow initiation sites. These other factors include the local slope,

which directly appears in the FOS equation, the soil composition, which affects the matric potential at saturation ψ_s, and the fractional vegetation cover V, which determines the vegetation cohesion. It also includes the soil moisture variation that is present in all scenarios. The importance of slope and vegetation in determining the debris flow initiation sites is consistent with the analysis of Rengers et al. (2016).

5. DISCUSSION

Overall, soil moisture can influence the initiation of debris flows through three pathways. First, as directly investigated in this study, if soil moisture is high at a particular location, it can promote instability and thus debris flow occurrence at that location. However, the results of this study suggest that the spatial pattern of soil moisture during the 2013 flood likely played a secondary role in determining the debris flow initiation locations. Second, soil moisture can affect debris flow occurrence by impacting the soil properties and vegetation patterns. Dry conditions are far more common in the Front Range than the wet conditions that occurred during the flood. During dry periods, topographic aspect and the associated patterns of insolation and potential ET tend to produce wetter conditions on NFS than SFS as demonstrated by the EMT+VS model. Over geologic time scales, this soil moisture pattern has likely helped produce different soil properties between the opposing hillslopes. Furthermore, the differences in microclimate, soil properties, and soil moisture have also likely resulted denser vegetation cover on NFS (Tinley, 1982). Thus, while the spatial pattern of soil moisture during the storm likely only had a secondary effect in determining the debris flow initiation sites, the soil moisture patterns during dry conditions probably had an indirect role in determining the debris flow initiation sites. Third, soil moisture also played an important role in determining the timing of the debris flows. Soil moisture is the only variable that changed in time in the EMT+VS model simulations, and instability occurred only after the coarse resolution soil moisture reached unusually high values.

6. CONCLUSIONS

The main objectives of this research were to determine if saturation was more common on SFS during the 2013 storm, to assess the hydrologic mechanisms that produced preferential saturation of SFS, and to evaluate the importance of the spatial pattern of soil moisture in determining the pattern of debris flow initiation. In-situ soil moisture observations from the Cache la Poudre catchment and Boulder Creek CZO were used to determine if saturation was more common on SFS. The EMT+VS model was then used to generate soil moisture patterns for five hypotheses including (1) higher rainfall rates, (2) lower interception rates, (3) lower porosity, (4) thinner soils, and (5) reduced deep drainage on SFS. An infinite slope stability model was then used to determine the soil stability for the different scenarios. The following conclusions can be derived from this study:

1. Saturation was more common on the SFS than NFS during the 2013 event. For the Cache la Poudre dataset, about 45% of the SFS locations saturated, while only about 9% of the NFS locations saturated during the storm. Similarly, for the Boulder Creek CZO dataset, approximately 40% of SFS sites saturated, while none of the NFS sites saturated during the storm. These results confirm the observations from Ebel et al. (2015). They also indicate that soil moisture patterns in the Front Range are temporally unstable. Although SFS were wetter than NFS during the storm, this pattern is reversed during normal dry conditions (Coleman and Niemann, 2013; Ranney et al., 2015).
2. The soil moisture maps from the EMT+VS model showed that differences in interception and deep drainage between NFS and SFS are sufficient to produce the reversal in the soil moisture pattern between the wet and dry conditions. During dry conditions, ET is the

dominant process in the soil's water balance. NFS have less ET than SFS due to shading of the soil by thicker vegetation and their orientation away from the sun. Thus, the soil is wetter on NFS. During wet conditions, lateral flow and deep drainage are the dominant processes. NFS have greater deep drainage due to the greater weathering of the bedrock. Increased deep drainage leads to drier soils. Interception is also greater on NFS due to the thicker vegetation cover. The greater interception leads to drier conditions on NFS than SFS in wet periods. The other hypotheses tested did not produce a reversal in the soil moisture pattern.

3. Although soil moisture was a key factor in determining when the debris flows occurred, the reversal of the soil moisture pattern likely played a secondary role in determining where the debris flows occurred. The base scenario, which does not include the reversal, predicted instability at 69.6% of the actual debris flow sites when a 30 m buffer is used. This high percentage suggests that other factors in the slope stability model (i.e. soil moisture variation in the base scenario, local slope, soil composition, and vegetation density) explain the instability at most locations. When the reversal is included in a combined scenario, instability is predicted at 71.6% of sites. This small increase likely also occurs because of inaccuracies in the estimated soil moisture pattern.

Several avenues are available for further research. Many inputs to the soil moisture and slope stability models were estimated from limited data. Thus, spatial variations in many soil and lithological properties were largely neglected in the analysis. It is expected that the performance of both models would improve with additional data collection for relevant properties throughout the Front Range. Improved performance might also be achieved by formal calibrations of the soil moisture and slope stability models. Both models have potential for application to other regions

and conditions. The EMT+VS model can potentially generate fine-resolution soil moisture patterns from ongoing satellite measurements of soil moisture for a variety of regions. Thus, slope stability could potentially be tracked in near real time using this soil moisture input. Finally, post-fire debris flows are an ongoing concern in some regions. These models could be extended to specifically consider both the hydrology and slope stability of post-fire conditions.

TABLES AND FIGURES

Table 1. EMT+VS model inputs and parameters for different scenarios

Parameters	Base Parameters	Precipitation	Interception	Soil Depth	Porosity	Deep Drainage	Combined
θ_s (m^3/m^3)	0.409	0.409	0.409	0.409	0.41-0.51	0.409	0.409
γ_h	14.4	14.4	14.4	14.4	14.4	14.4	14.4
γ_v	14.1	14.1	14.1	14.1	14.1	14.1	14.1
β_r	5.00	5.00	5.00	5.00	5.00	5.00	5.00
β_a	3.60	3.60	3.60	3.60	3.60	3.60	3.60
α	0.26	0.26	0.26	0.26	0.26	0.26	0.26
ε	1.33	1.33	1.33	1.33	1.33	1.33	1.33
η	0.04	0.04	0.04	0.04	0.04	0.04	0.04
$K_{s,v}$ (mm/day)	2529	2529	2529	2529	2529	556 – 4501	556 – 4501
ι	375	375	375	375	375	375	375
δ_0 (m)	0.60	0.60	0.60	0.56-0.64	0.60	0.60	0.56-0.64
$\kappa_{\min}$	-999999	-999999	-999999	-999999	-999999	-999999	-999999
λ	0	0	0.75	0	0	0	0.75
μ	1.92	1.92	1.92	1.92	1.92	1.92	1.92
$\overline{E}_p$ (mm/day)	2.15	2.15	2.15	2.15	2.15	2.15	2.15
ω (1/m)	0.000427	0.000427	0.000427	0.000427	0.000427	0.000427	0.000427
τ (1/m)	0	-0.00033	0	0	0	0	-0.00033
ξ	0	0.938	0	0	0	0	0.938
υ (degrees from north)	0	145	0	0	0	0	145

Table 2. Evaluation of the predicted maps of instability based on the different hypotheses

Cases	Observed Debris Flow Initiation Sites Calculated as Unstable by the Model	Observed Stable Locations Calculated as Stable by the Model
Base	69.6%	91.1%
Precipitation	69.2%	91.1%
Interception	70.8%	90.1%
Soil Depth	69.6%	91.1%
Porosity	47.9%	95.3%
Deep Drainage	71.4%	89.8%
Combined	71.6%	89.4%

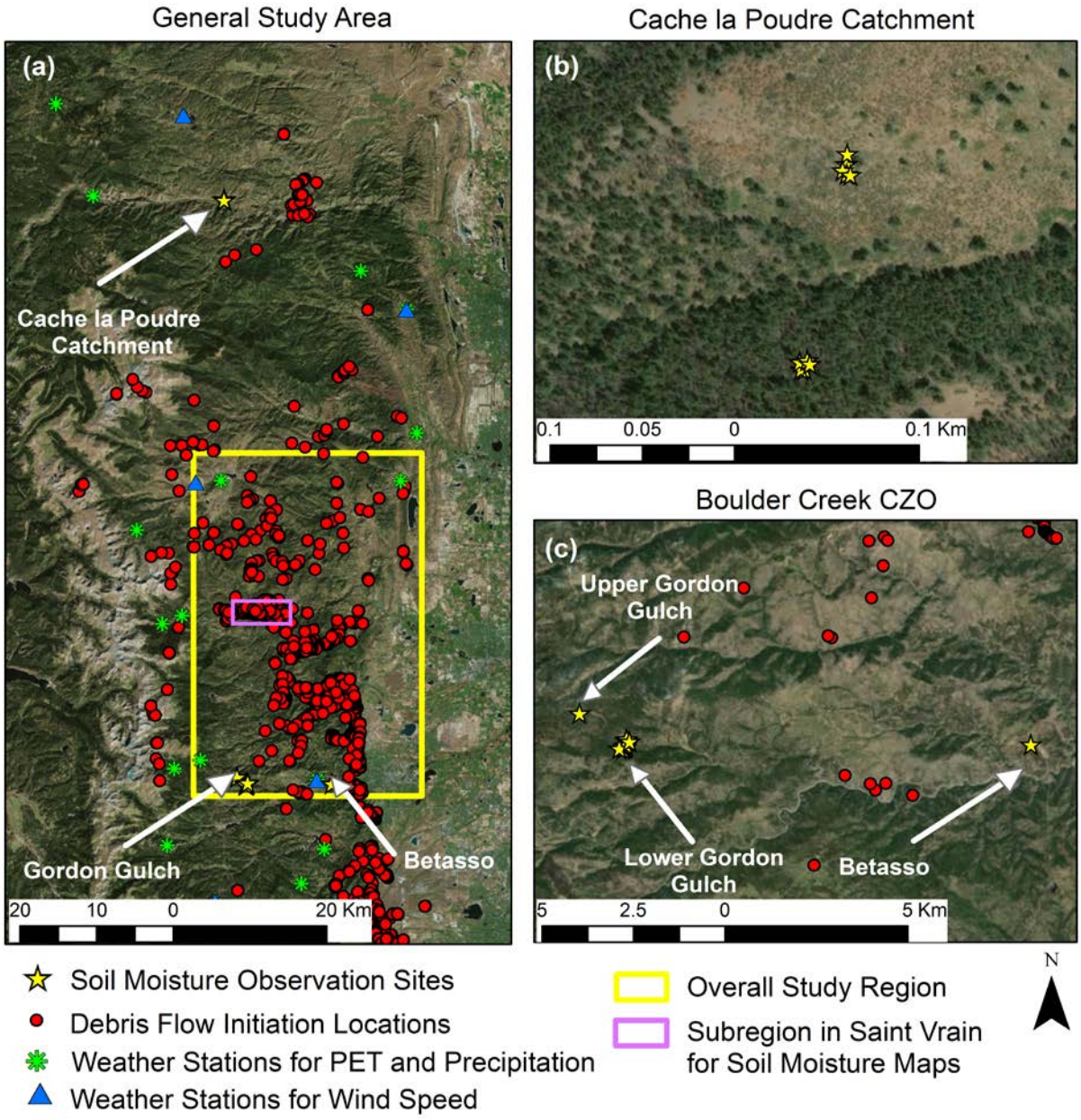

Figure 1. (a) Observed debris flow initiation sites, the overall study region, and a selected sub-region overlain on a satellite photo of the Front Range. Stations with soil moisture and other information are also shown. (b) Soil moisture observation sites in the Cache la Poudre catchment. (c) Soil moisture observation sites and mapped debris initiation sites in the Boulder Creek CZO area. Satellite Photo Source: ESRI, DigitalGlobe, Earthstar Geographics, CNES/Airbus DS, USDA, USGS, AeroGRID, IGN, and GIS User Community.

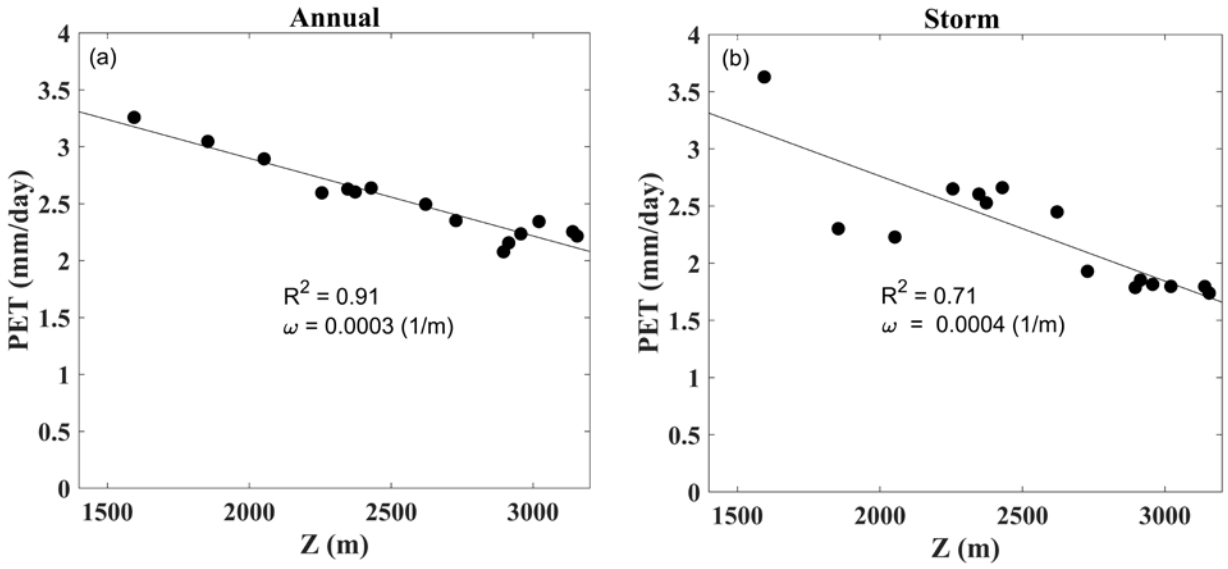

Figure 2. (a) Annual average PET and (b) storm-period average PET vs. elevation for the weather stations in the Front Range.

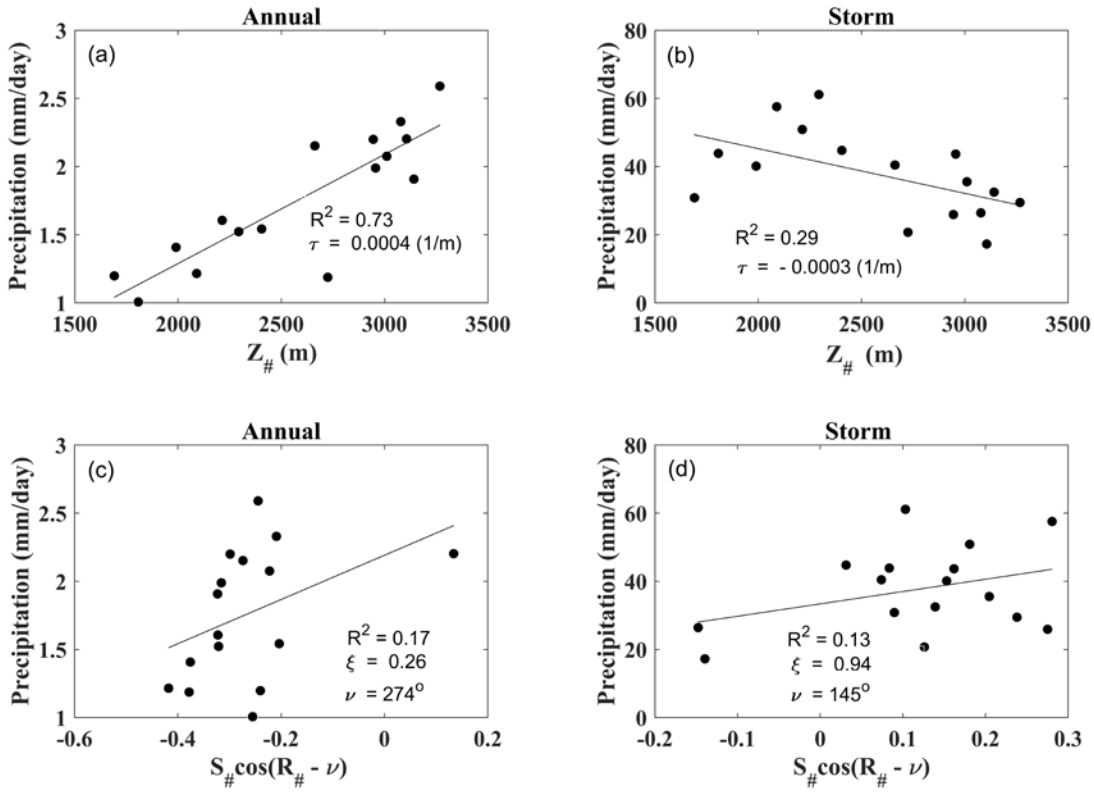

Figure 3. (a) Annual average precipitation rate vs. orographic-scale elevation $Z_{\#}$, (b) storm average precipitation rate vs. orographic-scale elevation $Z_{\#}$, (c) annual average precipitation rate vs. $S_{\#}\cos\left(R_{\#}-\nu\right)$, and (d) storm average precipitation rate vs. $S_{\#}\cos\left(R_{\#}-\nu\right)$.

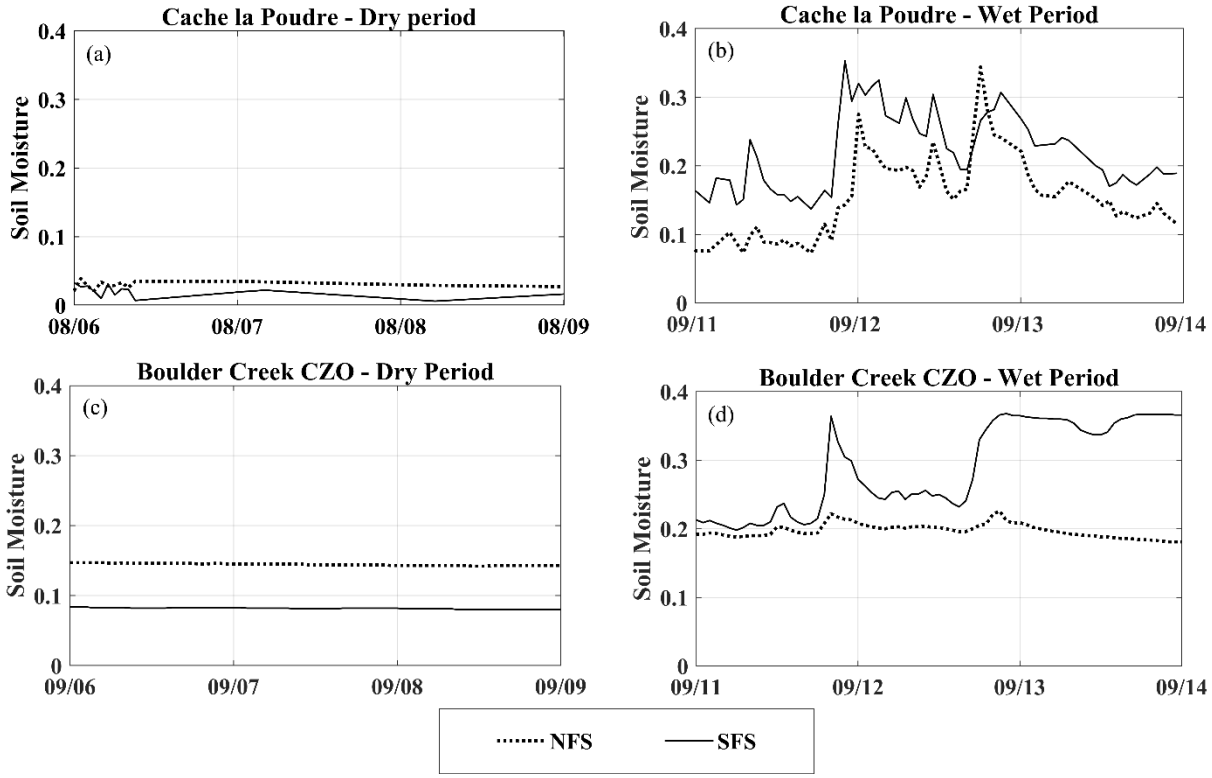

Figure 4. Soil moisture (m^3m^{-3}) through time for dry conditions before the storm and wet conditions during the storm on NFS and SFS at the Cache la Poudre catchment and Boulder Creek CZO.

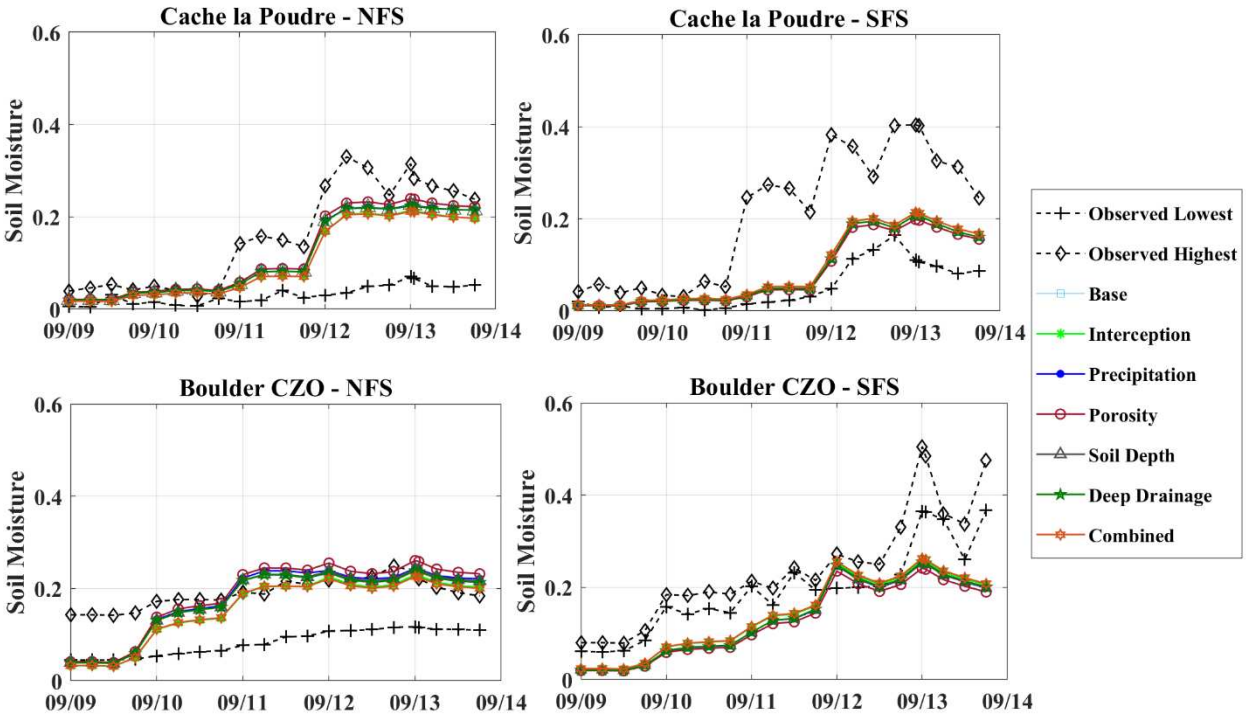

Figure 5. Observed soil moisture and EMT+VS soil moisture for different hypotheses during the storm period for NFS and SFS sites at the Cache la Poudre catchment and Boulder Creek CZO.

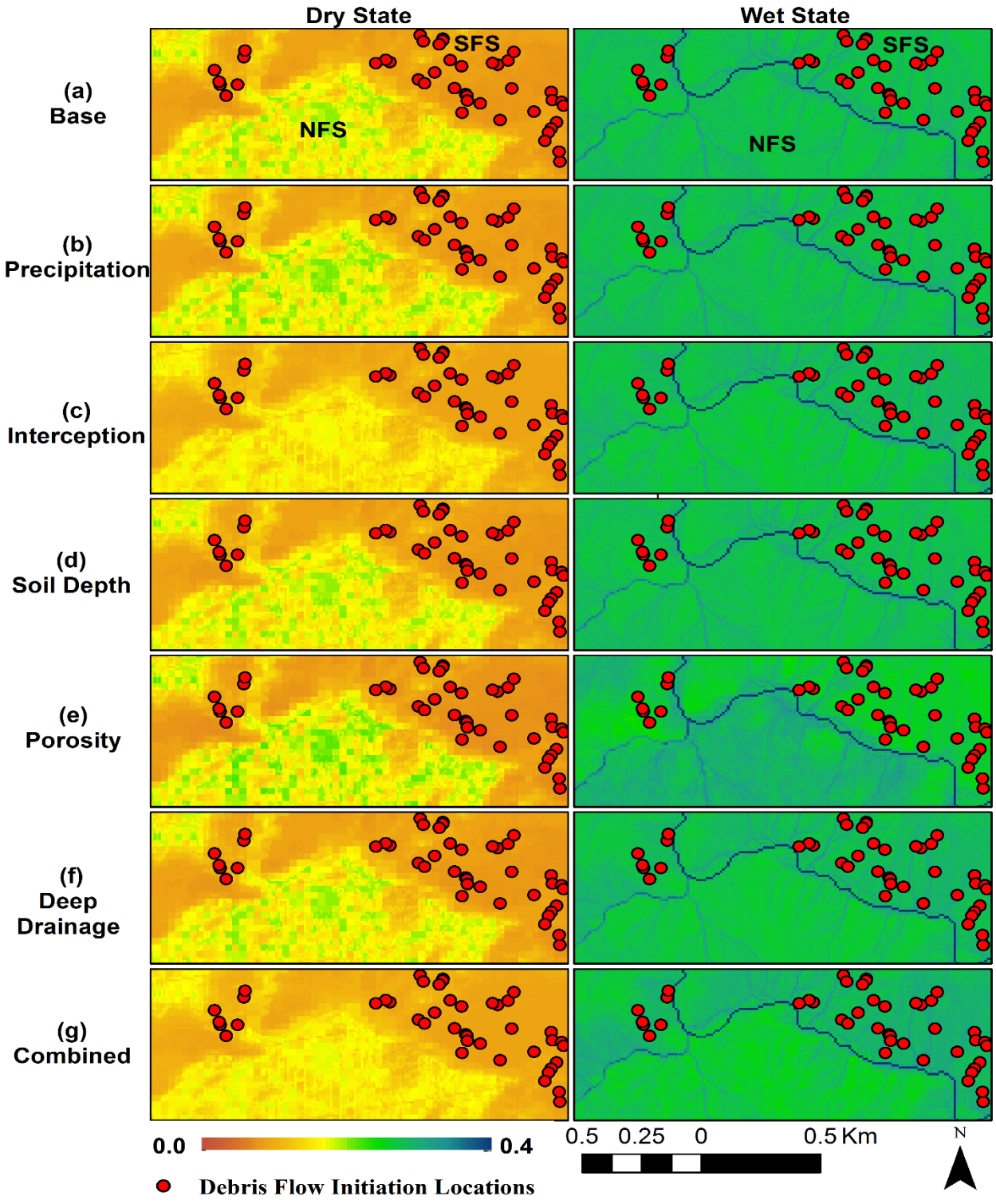

Figure 6. Soil moisture maps generated using different hypotheses for an example sub-region in the Saint Vrain watershed for the dry state (23:00 on 8 September 2013) and wet state (00:00 on 12 September 2013). Circles indicate mapped debris flow locations. The location and size of the sub-region is shown in Figure 1a.

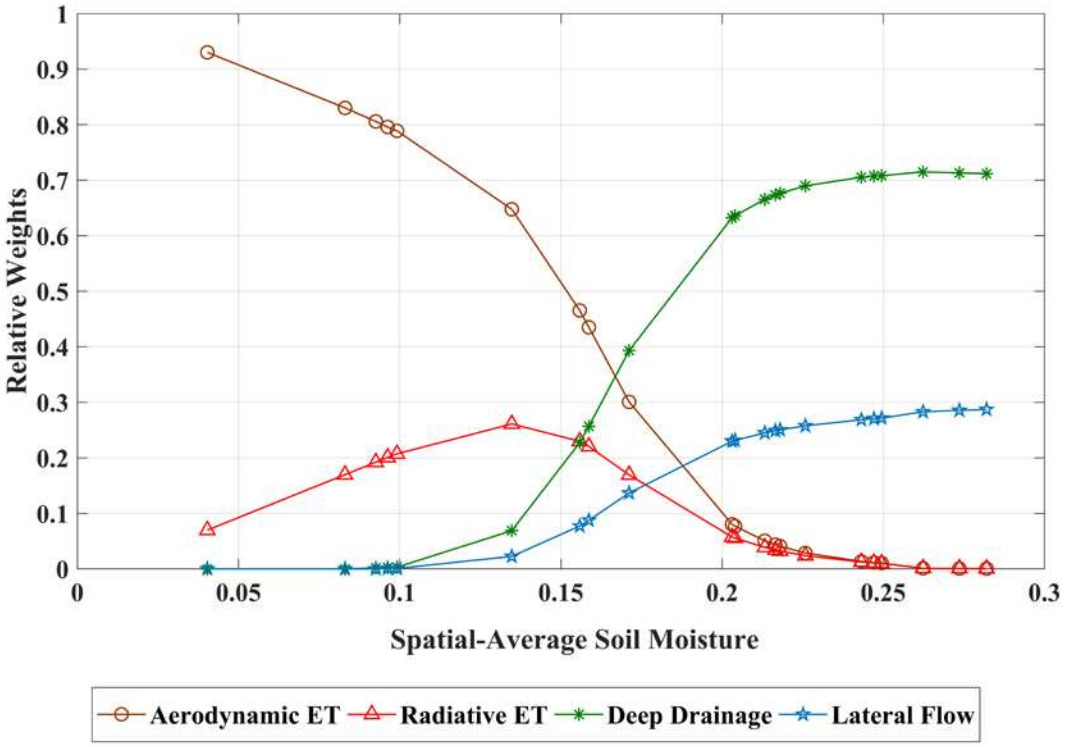

Figure 7. Relative weights as a function of the spatial average soil moisture from NLDAS showing the contributions of aerodynamic ET, radiative ET, deep drainage, and lateral flow in determining the soil moisture estimate.

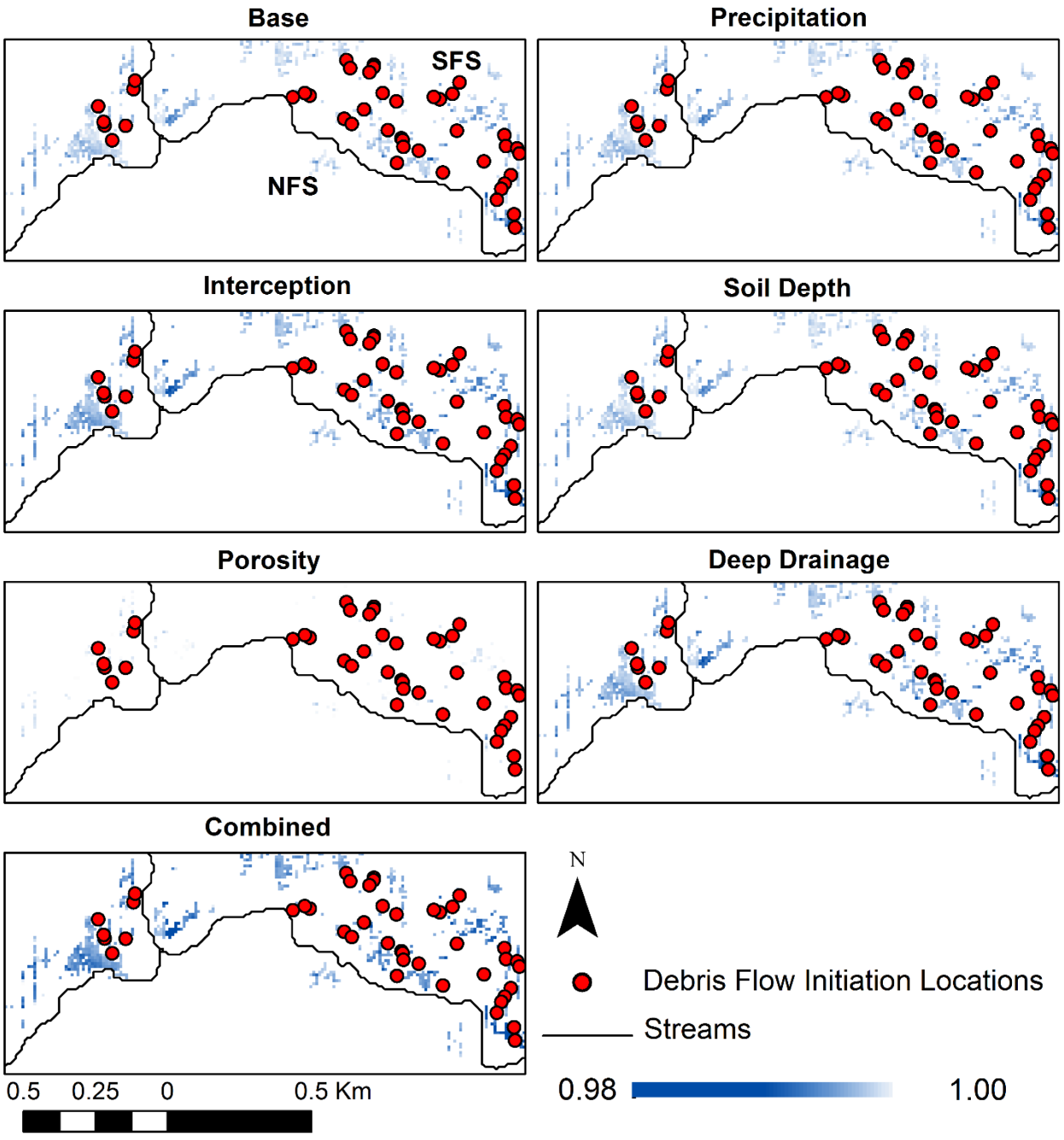

Figure 8. Factor of safety (FOS) maps generated by the slope stability model for the different hypotheses when applied to the example sub-region in the Saint Vrain watershed. FOS was calculated for 00:00 on 12 September 2013. The location and size of the sub-region is shown in Figure 1a.

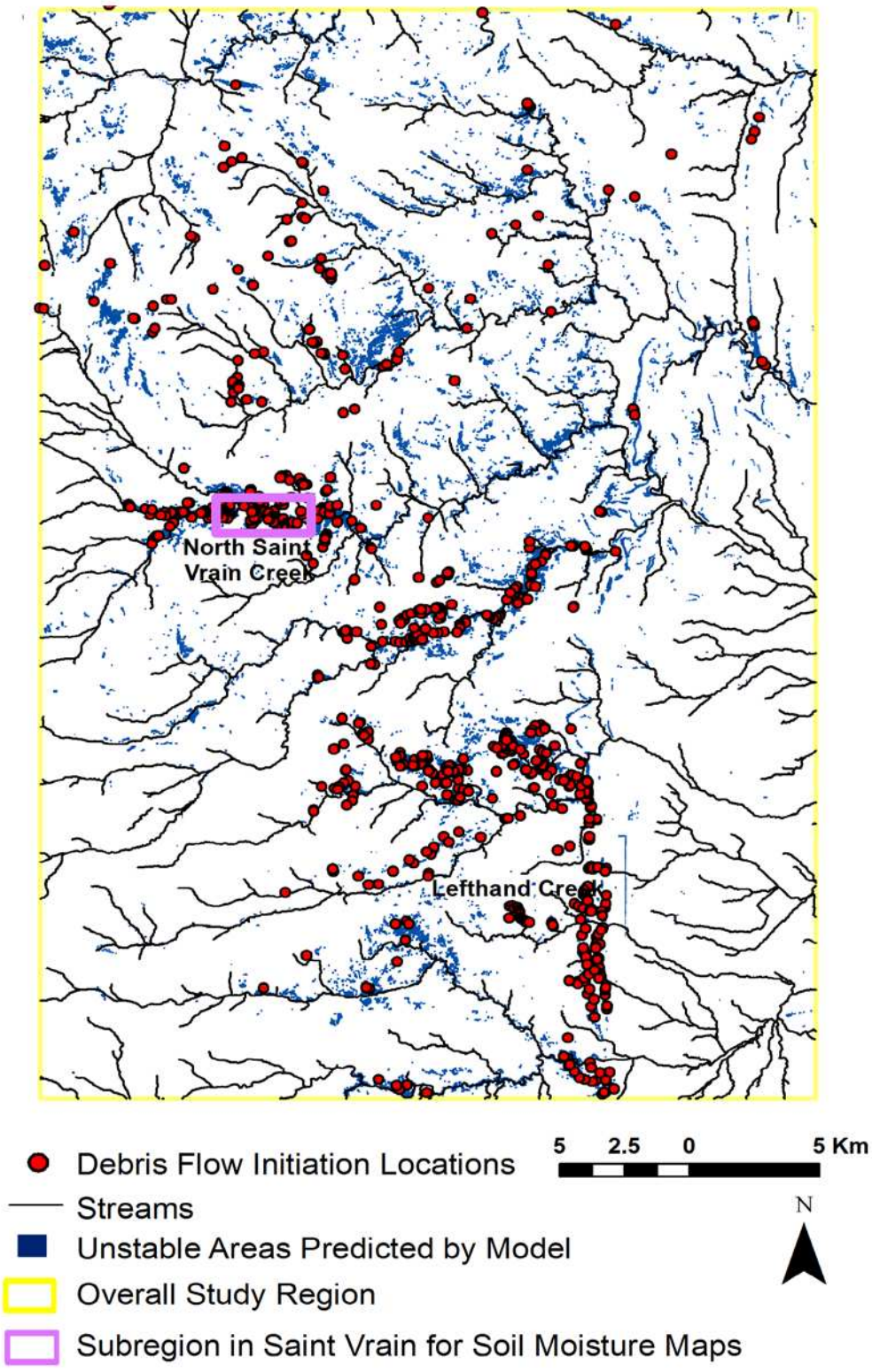

Figure 9. Factor of safety (FOS) maps generated by the slope stability model for the entire study region shown in Figure 1a.

REFERENCES

Anderson, S. P., Anderson, R. S., Hinckley, E. L. S., Kelly, P., & Blum, A. (2011). Exploring weathering and regolith transport controls on critical zone development with models and natural experiments. *Applied Geochemistry*, *26*, S3–S5. https://doi.org/10.1016/j.apgeochem.2011.03.014

Archer, N. A. L., Quinton, J. N., & Hess, T. M. (2002). Below-ground relationships of soil texture, roots and hydraulic conductivity in two-phase mosaic vegetation in South-east Spain. *Journal of Arid Environments*, *52*(4), 535–553. https://doi.org/10.1006/jare.2002.1011

Berglund, E. R., Ahyoud, A., & Tayaa, M. H. (1980). Comparison of soil and infiltration properties of range and afforested sites in northern Morocco. *Forest Ecology and Management*, *3*, 295–306.

Campbell, G. S. (1974). A simple method for determining unsaturated conductivity from moisture retention data. *Soil Science*, *117*(6), 311–314.

Carrara, A., Crosta, G., & Frattini, P. (2008). Comparing models of debris-flow susceptibility in the alpine environment. *Geomorphology*, *94*(3–4), 353–378. https://doi.org/10.1016/j.geomorph.2006.10.033

Coe, J. A., Kean, J. W., Godt, J. W., Baum, R. L., Jones, E. S., Gochis, D. J., & Anderson, G. S. (2014). New insights into debris-flow hazards from an extraordinary event in the Colorado Front Range. *GSA Today*, *24*(10), 4–10. https://doi.org/10.1130/GSATG214A.1

Coleman, M. L., & Niemann, J. D. (2013). Controls on topographic dependence and temporal instability in catchment-scale soil moisture patterns. *Water Resources Research*, *49*(3),

1625–1642. https://doi.org/10.1002/wrcr.20159

Coppin, Nick J., and I. G. R. (1990). *Use of vegetation in civil engineering (pp. 23-36)*. London: Construction Industry Research and Information Association.

Cosby, B. J., Hornberger, G. M., Clapp, R. B., & Ginn, T. R. (1984). A statistical exploration of the relationships of soil moisture characteristics to the physical properties of soils. *Water Resources Research*, *20*(6), 682–690.

Cowley, G. S., Niemann, J. D., Green, T. R., Seyfried, M. S., Jones, A. S., & Grazaitis, P. J. (2017). Impacts of precipitation and potential evapotranspiration patterns on downscaling soil moisture in regions with large topographic relief. *Water Resources Research*, *53*(2), 1553–1574. https://doi.org/10.1002/2016WR019907

Daly, C., Neilson, R. P., & Phillips, D. L. (1994). A statistical-topographic model for mapping climatological precipitation over mountainous terrain. *Journal of Applied Meteorology*, *22*(2), 140–158.

Ebel, B. A. (2012). Wildfire impacts on soil-water retention in the Colorado Front Range, United States. *Water Resources Research*, *48*(12), 1–12. https://doi.org/10.1029/2012WR012362

Ebel, B. A. (2013). Wildfire and aspect effects on hydrologic states after the 2010 Fourmile Canyon fire. *Vadose Zone Journal*, *12*(1), 0. https://doi.org/10.2136/vzj2012.0089

Ebel, B. A., Rengers, F. K., & Tucker, G. E. (2015). Aspect-dependent soil saturation and insight into debris-flow initiation during extreme rainfall in the Colorado front range. *Geology*, *43*(8), 659–662. https://doi.org/10.1130/G36741.1

Egli, M., Mirabella, A., & Sartori, G. (2008). The role of climate and vegetation in weathering and clay mineral formation in late Quaternary soils of the Swiss and Italian Alps. *Geomorphology*, *102*(3–4), 307–324. https://doi.org/10.1016/j.geomorph.2008.04.001

Geroy, I. J., Gribb, M. M., Marshall, H. P., Chandler, D. G., Benner, S. G., & Mcnamara, J. P. (2011). Aspect influences on soil water retention and storage. *Hydrological Processes*, *25*(25), 3836–3842. https://doi.org/10.1002/hyp.8281

Gochis, D., Schumacher, R., Friedrich, K., Doesken, N., Kelsch, M., Sun, J., … Brown, B. (2015). The great Colorado flood of September 2013. *Bulletin of the American Meteorological Society*, *96*(9), 1461–1487. https://doi.org/10.1175/BAMS-D-13-00241.1

Gray, D. ., & Megahan, W. . (1981). Forest vegetation removal and slope stability in the Idaho Batholith. *USDA For. Serv. Res. Pap*, *271*, 11–19.

Grieco, N. R., Niemann, J. D., Green, T. R., Jones, A. S., & Grazaitis, P. J. (2018). Hydrologic Downscaling of Soil Moisture Using Global Data Sets without Site-Specific Calibration. *Journal of Hydrologic Engineering*, *23*(11), 4018048. https://doi.org/10.1061/(asce)he.1943-5584.0001702

Hinckley, E. L. S., Ebel, B. A., Barnes, R. T., Anderson, R. S., Williams, M. W., & Anderson, S. P. (2014). Aspect control of water movement on hillslopes near the rain-snow transition of the Colorado Front Range. *Hydrological Processes*, *28*(1), 74–85. https://doi.org/10.1002/hyp.9549

Hoehn, D. C. (2016). *Downscaling soil moisture over regions that include multiple coarse-resolution grid cells*. Colorado State University.

Jarrett, R. . D. (1990). Hydrologic and hydraulic research in mountain rivers 1. *JAWRA Journal of the American Water Resources Association*, *26*(3), 419–429. https://doi.org/10.1111/j.1752-1688.1990.tb01381.x

Lu, N., & Godt, J. (2008). Infinite slope stability under steady unsaturated seepage conditions. *Water Resources Research*, *44*(11). https://doi.org/10.1029/2008WR006976

Marr, J. W. (1961). Ecosystems of the East Slope of the Front Range in Colorado. *University of Colorado Studies, Seiries in Biology 8*, 144. https://doi.org/10.2307/2483242

Matsui, T., Lakshmi, V., & Small, E. E. (2005). The effects of satellite-derived vegetation cover variability on simulated land-atmosphere interactions in the NAMS. *Journal of Climate*, *18*(1), 21–40. https://doi.org/10.1175/JCLI3254.1

McCulloch, J. S. G., & Robinson, M. (1993). History of forest hydrology. *Journal of Hydrology*, *150*(2–4), 189–216. https://doi.org/10.1016/0022-1694(93)90111-L

McGuire, L. A., Rengers, F. K., Kean, J. W., Coe, J. A., Mirus, B. B., Baum, R. L., & Godt, J. W. (2016). Elucidating the role of vegetation in the initiation of rainfall-induced shallow landslides: Insights from an extreme rainfall event in the Colorado Front Range. *Geophysical Research Letters*, *43*(17), 9084–9092. https://doi.org/10.1002/2016GL070741

Montandon, L. M., & Small, E. E. (2008). The impact of soil reflectance on the quantification of the green vegetation fraction from NDVI. *Remote Sensing of Environment*, *112*(4), 1835–1845. https://doi.org/10.1016/j.rse.2007.09.007

Montgomery, D. R., & Dietrich, W. E. (1994). A physically based model for the topographic control on shallow landsliding. *Water Resources Research*, *30*(4), 1153--1171.

Nikiforoff, C. C. (1949). Weathering and soil evolution. *Soil Science*, *67*(3), 219–230. https://doi.org/10.1097_00010694-194903000-00003

Patton, A. I., Rathburn, S. L., Bilderback, E. L., & Lukens, C. E. (2018). Patterns of debris flow initiation and periglacial sediment sourcing in the Colorado Front Range. *Earth Surface Processes and Landforms*, *43*(15), 2998–3008. https://doi.org/10.1002/esp.4463

Petersson, H., Messing, I., & Steen, E. (1987). Influence of root mass on saturated hydraulic conductivity in arid soils of central Tunisia. *Arid Land Research and Management*, *1*(3),

149–160. https://doi.org/10.1080/15324988709381140

Priestley R.J, C. H. B. and T. (1972). On the assessment of surface heat flux and evaporation using large-scale parameters. *Monthly Weather Review*, *100*(2), 81–92.

Ranney, K. J., Niemann, J. D., Lehman, B. M., Green, T. R., & Jones, A. S. (2015). A method to downscale soil moisture to fine resolutions using topographic, vegetation, and soil data. *Advances in Water Resources*, *76*, 81–96. https://doi.org/10.1016/j.advwatres.2014.12.003

Rasse, D. P., Smucker, A. J. M., & Santos, D. (2000). Alfalfa root and shoot mulching effects on soil hydraulic properties and aggregation. *Soil Science Society of America Journal*, *64*(2), 725–731. https://doi.org/10.2136/sssaj2000.642725x

Reichenbach, P., Rossi, M., Malamud, B. D., Mihir, M., & Guzzetti, F. (2018). A review of statistically-based landslide susceptibility models. *Earth-Science Reviews*, *180*(November), 60–91. https://doi.org/10.1016/j.earscirev.2018.03.001

Rempe, D. M., & Dietrich, W. E. (2014). A bottom-up control on fresh-bedrock topography under landscapes. *Proceedings of the National Academy of Sciences*, *111*(18), 6576–6581. https://doi.org/10.1073/pnas.1404763111

Rengers, F. K., McGuire, L. A., Coe, J. A., Kean, J. W., Baum, R. L., Staley, D. M., & Godt, J. W. (2016). The influence of vegetation on debris-flow initiation during extreme rainfall in the northern Colorado Front Range. *Geology*, *44*(10), 823–826. https://doi.org/10.1130/G38096.1

Schmidt, K. M., Roering, J. J., Stock, J. D., Dietrich, W. E., Montgomery, D. R., & Schaub, T. (2001). The variability of root cohesion as an influence on shallow landslide susceptibility in the Oregon Coast Range. *Canadian Geotechnical Journal*, *38*(5), 995–1024. https://doi.org/10.1139/t01-031

Sharples, J. J., Hutchinson, M. F., & Jellett, D. R. (2005). On the horizontal scale of elevation dependence of Australian monthly precipitation. *Journal of Applied Meteorology*, *44*(12), 1850–1865. https://doi.org/10.1175/jam2289.1

Smith, T. J., Mcnamara, J. P., Flores, A. N., Gribb, M. M., Aishlin, P. S., & Benner, S. G. (2011). Small soil storage capacity limits benefit of winter snowpack to upland vegetation. *Hydrological Processes*, *25*(25), 3858–3865. https://doi.org/10.1002/hyp.8340

Tang, W. H., Stark, T. D., & Angulo, M. (1999). Reliability in back analysis of slope failures. *Soils and Foundations*, *39*(5), 73–80.

Tarboton, D. (2003). Terrain Analysis Using Digital Elevation Models in Hydrology. *In 23rd ESRI International Users Conference, San Diego, California*, *14*.

Thornton, P. E., Running, S. W., & White, M. A. (1997). Generating surfaces of daily meteorological variables over large regions of complex terrain. *Journal of Hydrology*, *190*(3–4), 214–251. https://doi.org/10.1016/S0022-1694(96)03128-9

Tinley, K. . (1982). The influence of soil moisture balance on ecosystem patterns in southern Africa. *Ecology of Tropical Savannas*, 175–192. Springer, Berlin, Heidelberg.

Tiwari, B., Brandon, T. L., Marui, H., & Tuladhar, G. R. (2005). Comparison of residual shear strengths from back analysis and ring shear tests on undisturbed and remolded specimens. *Journal of Geotechnical and Geoenvironmental Engineering*, *131*(9), 1071–1079. https://doi.org/10.1061/(asce)1090-0241(2005)131:9(1071)

Traff, D. C., Niemann, J. D., Middlekauff, S. A., & Lehman, B. M. (2015). Effects of woody vegetation on shallow soil moisture at a semiarid montane catchment. *Ecohydrology*, *8*(5), 935–947. https://doi.org/10.1002/eco.1542

Valante, F., David, J. S., & Gash, J. H. C. (1997). Modelling interception loss for two sparse

eucalypt and pine forests in central Portugal using reformulated Rutter and Gash analytical models. *Journal of Hydrology*, *190*(1–2), 141–162. https://doi.org/10.1016/S0022-1694(96)03066-1

Western, A. W., Grayson, R. B., Bschl, G., & Willgoose, G. R. (1999). Western et al. 1999 - Observed spatial organization of soil moisture and its relation to terrain indices. *Water Resources Research*, *35*(3), 797–810.

White, T., Brantley, S., Banwart, S., Chorover, J., Dietrich, W., Derry, L., … McDowell, B. (2015). The Role of Critical Zone Observatories in Critical Zone Science. In *Developments in Earth Surface Processes* (Vol. 19). https://doi.org/10.1016/B978-0-444-63369-9.00002-1

Wilson, M. J. (2004). Weathering of the primary rock-forming minerals: processes, products and rates. *Clay Minerals*, *39*(3), 233–266. https://doi.org/10.1180/0009855043930133

Wu, T. H., McKinnell III, W. P., & Swanston, D. N. (1979). Strength of tree roots and landslides on Prince of Wales Island, Alaska. *Canadian Geotechnical Journal*, *16*(1), 19–33. https://doi.org/10.1139/t79-003

Xia, Y., Ek, M. B., Wu, Y., Ford, T., & Quiring, S. M. (2015). Comparison of NLDAS-2 Simulated and NASMD Observed Daily Soil Moisture. Part I: Comparison and Analysis. *Journal of Hydrometeorology*, *16*(5), 1962–1980. https://doi.org/10.1175/JHM-D-14-0096.1

Xia, Y., Mitchell, K., Ek, M., Sheffield, J., Cosgrove, B., Wood, E., … Mocko, D. (2012). Continental-scale water and energy flux analysis and validation for the North American Land Data Assimilation System project phase 2 (NLDAS-2): 1. Intercomparison and application of model products. *Journal of Geophysical Research Atmospheres*, *117*(3). https://doi.org/10.1029/2011JD016048

Zeng, X., Dickinson, R. E., Walker, A., Shaikh, M., DeFries, R. S., & Qi, J. (2000). Derivation and evaluation of global 1-km fractional vegetation cover data for land modeling. *Journal of Applied Meteorology*, *39*(6), 826–839. https://doi.org/10.1175/1520-0450(2000)039<0826:daeogk>2.0.co;2

Zhang, J., Tang, W. H., & Zhang, L. M. (2009). Efficient probabilistic back-analysis of slope stability model parameters. *Journal of Geotechnical and Geoenvironmental Engineering*, *136*(1), 99–109. https://doi.org/10.1061/(asce)gt.1943-5606.0000205

Ziemer, R. (n.d.). The role of vegetation in the stability of forested slopes. *In Proceedings of the International Union of Forestry Research Organizations, XVII World COngress, 6-17 September 1981, Kyoto, Japan*, *I*, 297–308.